이 학 석 사 학 위 논 문

Characterizing Polarization-dependent Optical Properties of Single Anisotropic Gold Nanoparticles

단일 비등방성 금 나노 입자의 편광 의존성 광학적 특성 분석

울 산 대 학 교 대 학 원

화 학 과

이 준 호

Characterizing Polarization-dependent Optical Properties of Single Anisotropic Gold Nanoparticles

지 도 교 수: 하 지 원

이 논문을 이학 석사 학위 논문으로 제출함

2019年 2月

울 산 대 학 교 대 학 원

화 학 과

이 준 호

이 준 호의 이학 석사 학위 논문을 인준함

심사위원 하 지 원 인

심사위원 이 영 일 인

심사위원 김 용 수 인

울 산 대 학 교 대 학 원

2019년 2월

Korean Abstract

금, 은, 구리와 같은 귀금속 나노 입자들은 독특한 광학적 특성을 나타낸다. 특히나 금 나노 입자는 크기, 모양, 주변 매질의 굴절률에 따라 달라지는 국지 표면 플라즈몬 공명 (Localized Surface Plasmon Resonance, LSPR) 이라는 독특한 광학적 특성을 지니고 있다. 더불어 합성 시 크기와 모양의 조절이 쉬우며 표면 개질이 쉽고, 생체 적합성을 가지기 때문에 다양한 분야에서 활용되고 있다. 현재까지 대부분의 연구는 집합체 수준에서의 금 나노 입자의 특성을 분석하였다. 하지만 금 나노 입자의 광학적 특성을 더 깊이 이해하고 광학 탐침, 센서, 약물 전달체 등 다양한 분야에서보다 넓은 활용을 위해서는 집합체 평균 없이 나노 입자의 단일 입자 수준에서의 연구가 더욱 필요하다.

본 실험에서는 암시야 현미경을 이용하여, 비등방성 모양을 가진 금 나노 입자의 광학적 특성을 단일 입자 수준에서 분석하였다. 비등방성 모양을 가진 금 나노 입자는 그 모양 때문에 편광의 방향에 따라 달라지는 광학적 특성을 나타내게 된다. 크기가 빛의 파장보다 큰 막대모양의 금 마이크로 입자를 암시야 현미경을 이용하여 초점, 비초점, 산란 이미지와 스펙트럼을 얻었다. 암시야 현미경을 이용한 비초점 이미지를 통해 막대 모양의 금 마이크로 입자의 단일 다이폴(dipole)의 산란을 측정하였고, 도넛 모양의 이미지 패턴이 나타나는 것을

확인하였다. 또한 삼각형 모양의 금 나노 입자는 종횡비에 따라 나타나는 Quadrupole resonance mode와 Dipole resonance mode를 확인 할 수 있었고, 편광의 각도에 따라 달라지는 이미지 패턴 및 신호세기의 변화를 확인하였다. 이를 통해 본 논문에서는 비등방성 나노입자들의 광학적 특성 규명 뿐만 아니라 다 기능성 광학 탐침, 센서 등 다양한 분야에서의 응용 가능성을 제시하였다.

English Abstract

Precious metal nanoparticles such as gold, silver, and copper exhibit unique optical properties. In particular, gold nanoparticles have a unique optical property called Localized Surface Plasmon Resonance (LSPR), which depends on the size, shape, and refractive index of the surrounding medium. In addition, it is easy to control the size and shape during synthesis, it is easy to modify the surface and has biocompatibility, so it is used in various fields. To date, most studies have analyzed the properties of gold nanoparticles at the ensemble level. However, in order to better understand the optical properties of gold nanoparticles and to make wider use in various fields such as optical probes, sensors, drug delivery systems, etc., research at single particle level of nanoparticles is needed even without ensemble averaging.

In this experiment, the optical properties of gold nanoparticles with anisotropic shape were characterized at a single particle level using a dark-field (DF) microscope. Anisotropic gold nanoparticles exhibit optical properties that depend on the direction of polarization due to their shape. Focused and defocused scattering images and scattering spectra were obtained using a DF microscope for large gold microrods. A donut-shaped scattering image pattern of gold microrods was observed, and the defocused image pattern allowed us to measure spatial field distribution from gold microrods. In addition, we investigated the optical properties of triangular gold nanoplates at the single particle level under DF microscopy. The quadrupole resonance mode and the dipole resonance mode of the triangular gold nanoparticles confirmed were gold nanoplates with aspect ratio of ~ 5 (edge length: 100.4 nm, thickness: 21.1

nm), and the polarization-dependent optical characteristics were revealed through the defocused scattering image patterns according to the polarization direction of incident light. Therefore, we provide the possibility of using anisotropic gold nanoparticle in many applications such as multifunctional optical probe, sensor, etc..

Index

Figure index

1. Introduction

Plasmonic nanoparticles (NPs) have gained great attention in respect to their localized surface plasmon resonance (LSPR) property and potential applications in various fields. LSPR is coherent oscillations of the conduction band electron induced by interaction with electromagnetic field. LSPR is highly sensitive to the shapes, materials and surrounding medium of metal NPs. The LSPR wavelength can be conveniently controlled by varying the aspect ratio and surrounding medium of the nanoparticles [1, 2]. In particular, gold nanoparticles are being studied in a variety of fields including drug delivery systems[3, 4], photo-thermal therapy[5, 6], chemical sensor[7-9], and optical probes[10, 11], because they can be controlled in size and shape during synthesis[12], are not toxic[13], and are easy to modify. Furthermore, their tips which are well established to increase the enhancement due to the concentrated electric fields at sharpened features and edges, and allows single particles to function as highly sensitive SERS substrate [14]. Due to the unique optical properties of these gold nanoparticles due to LSPR, many studies have been carried out in various fields, but these studies have mostly been conducted at the ensemble level. When metal nanoparticles are studied at the ensemble level, their optical properties are predicted by the average value of nanoparticles of different sizes and shapes. However, the unique optical properties caused by the LSPR are affected by the shape and size of the metal nanoparticles and the refractive index of the surrounding medium. Therefore, studies at a single particle level are essential to have deeper understanding of their optical properties [15].

A variety of imaging techniques have been employed to visualize gold nanoparticles and to investigate their optical properties at the single particle level. The optical imaging techniques include dark-field (DF) microscopy[11], photothermal heterodyne imaging[16], differential interference contrast microscopy[10, 17], total internal reflection microscopy[18] and surface enhanced Raman spectroscopy [19, 20]. In this experiment, optical properties of gold microrods (AuMRs) and triangular gold nanoplates (AuNPs) were characterized at single particle level using DF microscope. The DF microscope blocks external light from entering the objective lens, and only the light scattered by the sample is selectively collected by the objective lens, resulting in a dark background image and a brightly spot of a nanoparticle. This allows simple and efficient measurement of optical properties at the single particle level without ensemble averaging. In addition, the defocused orientation imaging (DOI) technique, which intentionally defocuses the DF image obtained through the DF microscope, can be used to determine the orientation of the gold nanoparticles in three dimensions without any degeneracy [21, 22].

In recent years, there have been many research efforts to investigate the optical properties of AuMRs at the single particle level. However, there have been no reports on the characterization of the optical properties of single AuMRs using defocused DF microscopy. The main advantage of using micrometer-long AuMRs in many applications is that their in-plane orientations and motions can be directly visualized by eye under an optical microscope, which differs from gold nanorods (AuNRs) much smaller than the wavelength of light. However, it is still challenging to determine the

three-dimensional (3D) orientation (in-plane and out-of-plane angles) of single AuMRs by eye. In this regard, it is necessary to gain a deeper insight into the optical properties and characteristic defocused DF image patterns of micrometer-long AuMRs at the single particle level. Furthermore, it is required to develop an accurate method to resolve the out-of-plane angles of single AuMRs with optical microscopy.

Besides, the one-dimensional (1D) gold nanoparticles, two dimensional (2D) triangular gold nanoplates (AuNPs) with sharp edges and tips have recently obtained increased attention due to their characteristic LSPR optical properties. For example, unlike 1D gold nanoparticles, the 2D triangular AuNPs exhibit two typical LSPR modes of dipole resonance mode and quadrupole resonance mode in the visible and near-infrared (IR) regions. The most important factor to determine LSPR modes in the 2D AuNPs has been reported to be an aspect ratio determined by their edge length and thickness. For example, Shuford et al. demonstrated that optical properties of single AuNPs are dependent on the triangular edge length and the plate thickness [23]. Furthermore, typical quadrupole resonance mode and dipole resonance mode cannot be clearly observed for thick or obtuse AuNPs, and the LSPR wavelength from dipole resonance is red-shifted with increasing of the edge length at a fixed thickness. At the constant edge length, the LSPR wavelength from dipole resonance is red-shifted with decreasing of the thickness. Despite the recent studies on the 2D AuNPs, our understanding of their optical properties is still very limited at the single particle level.

In the present study, we investigated single AuMRs under a defocused DF microscope in an attempt to better understand the effect of the defocus aberration on

the DF scattering image patterns. We further tested if we could resolve the out-of-plane angle of a AuMR under a defocused DF microscope. The defocused DF orientation imaging technique (DOI) is based on the direct detection of the spatial distribution of the scattered or emitted field of single dipoles when an aberration is deliberately applied to the imaging system. Furthermore, we synthesized triangular AuNPs with an average edge length of 100.4 nm and an average thickness of 21.1 nm through a one-pot seedless growth method and characterized their optical properties at the single particle level under DF scattering microscopy and spectroscopy. Furthermore, we demonstrated polarization-dependent, periodic defocused DF image patterns and intensities of single AuMRs and triangular 2D AuNPs.

2. Experimental Section

2.1. Material and Instrumentation

Gold microrods (AuMRs) with an average size of 200 nm × 1 μm used in the experiment was purchased from Sigma-Aldrich, and 1-decanethiol, p-aminothiophenol and p-nitrothiophenol were also purchased from Sigma-Aldrich. The Au nanoparticles were characterized via scanning electron microscopy (SEM), and we confirmed LSPR of Au nanoparticles at the ensemble level by UV-Vis spectroscope.

The single particle analysis of metal nanoparticles mainly was carried out under a DF microscope equipped with a spectrograph and CCD camera. DF images were obtained using a Nikon inverted microscope (ECLIPSE Ti-U). In the DF mode, a Nikon Plan Flour 100 × 0.5-1.3 oil iris objective lens and a condenser lens were used. Using the Andor iXonEM + CCD camera (iXon Ultra 897), we got images of gold nanoparticles. Images obtained through a DF microscope were analyzed using the Image J program. DF scattering spectra were obtained using a microscope combining an Andor spectrometer (SHAMROCK 303I, SR-303I-A) and an Andor CCD camera (Newton DU920P-OE). The DF microscope can obtain images in which the light irradiated on the sample does not enter the objective lens, only the light scattered by the sample enters the objective lens, and the background is dark and only the sample bright. The scattered light enters the entrance of the spectrometer and is dispersed by

grating (300 l / mm). Figure 1 shows working principle of DF microscopy. The spectra were obtained and analyzed through MATLAB program.

2.2. Sample Preparation

We cleaned the microscope cover glasses and slide glasses by first sonicating in ethanol for 15 min, in acetone for 5 min, and then in methanol for 15 min with intermediate steps of N_2 blow drying. We sonicated the solution containing Au nanoparticles for 5 min in order to prevent the aggregation of the nanoparticles. A sample was then prepared by drop casting the Au nanoparticle solution onto the pre-cleaned glass slides. The concentration of Au nanoparticles on the glass surface was controlled to be about 1 μm^{-2} to facilitate single nanoparticle characterization and to minimize inter-particle LSPR coupling. Then, the Au nanoparticles solution was sandwiched between a ranged pre-cleaned slide glass and a cover glass.

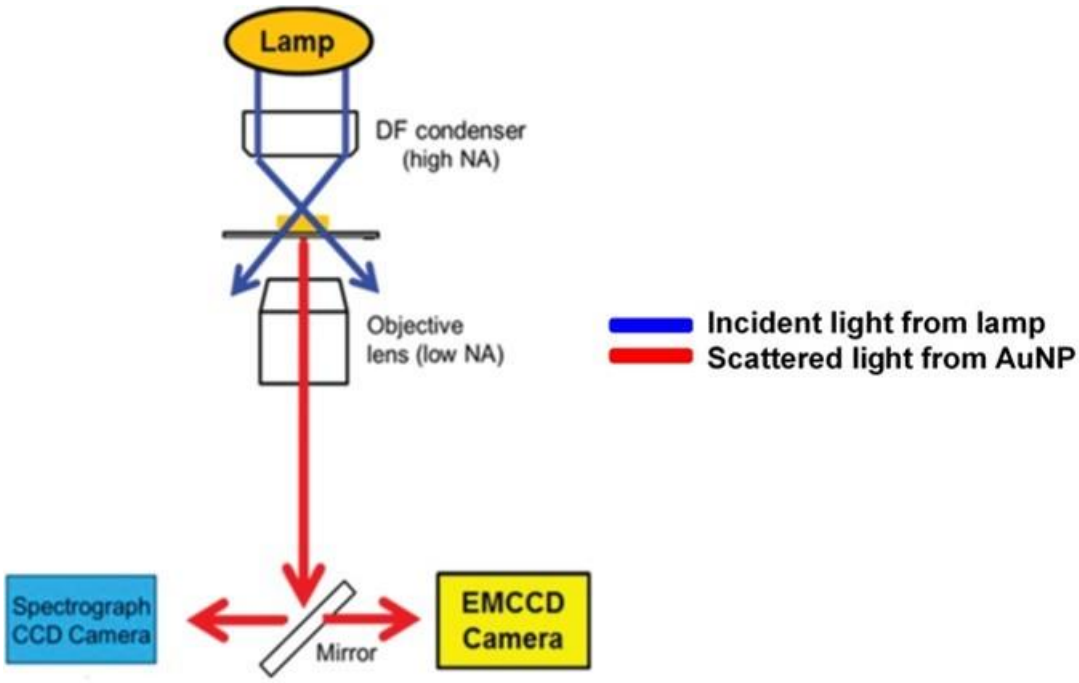

Figure 1. Illustration of dark-field (DF) microscopy

2.3. Defocused Scattering Microscopy

The sample glass slide was placed onto the microscope stage. The focused and defocused DF images of single Au nanoparticles were obtained by using a motorized rotary stage from Sigma Koki (SGSP-60YAM) coupled to the fine-adjustment knob on the microscope. The motor was controlled by Intelligent Driver, CSG-602R (Sigma Koki). We scanned in the z-direction with a vertical step size of ~ 40 nm. The vertical scan allowed us to obtain both focused and defocused images of single Au nanoparticles deposited on a glass slide at a different defocusing distance.

2.4. Simulation of Scattering Image pattern of Gold Microrods

We used the simulation program developed by Enderlein and Böhmer. The program is designed to calculate the characteristic intensity distribution from an emitter with three perpendicular emission oscillations of different emission strength. It has been widely used to determine the spatial orientation of single dye molecules. The simulation program is a special MATLAB based utility with a graphics user interface (GUI) for easy calculation. This program allows us to calculate exactly the defocused (or focused) images of single molecules.

The parameters that can be input are: the numerical aperture of the objective lens, magnification of imaging, extent of defocusing (or defocusing distance in micrometers), κ and R. For defining the emission strength ratios of the three independent oscillations (Figure 2), we input the parameter κ and R into the program.

The ratio κ defines the ratio of the emission strength of the b- to the c-oscillation (transverse oscillations, Figure 2) as shown below.

$$I_b / I_c = (1-\kappa)/(1+\kappa)$$

In this study the emission strength of the b-oscillation is assumed to be same as that of the c-oscillation. In addition, the ratio R defines the emission strength of the a-oscillation (or longitudinal oscillation) to the combined b and c oscillations (or transverse oscillations) as shown below.

$$R \times I_a + (1-R) \times (I_b + I_c)$$

When R is 1, we only have the contribution from a-oscillation (longitudinal oscillation) to the image patterns. However, the other two transverse oscillations (b and c) start to contribute to the image patterns with decreasing the ratio R. That is, lower R values indicate more contributions from the two transverse oscillations. Therefore, we were able to calculate the scattering patterns of AuMRs by adjusting the important parameters.

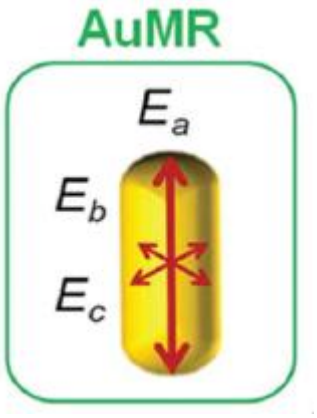

Figure 2. A schematic depicting three-perpendicular oscillations along the three axes. Ea denotes the scattering electric field of the microrod along the main long axis.

2.5. Effect of Electrophilicity of Adsorbed Thiol Molecules on LSPR Peak Shift in Gold Microrods

In the experiment of attaching thiol groups to AuMRs, thiol molecules do not dissolve in water. Therefore, AuMRs were dropped and dispersed on the above-mentioned washed slide glass, and the dispersed solution is completely dried through a dry keeper. Thiol molecules are then diluted in ethanol, drop cast onto a completely dry slide glass, and then the cover glass is sealing. Thereafter, the mixture is allowed to stand at room temperature for 30 minutes so that the thiol molecules and gold are completely reacted. For experiments that observe changes in the LSPR peak of AuMRs over time, the sample was fixed on the stage and focused, then the ethanol inside the sample was completely dried and then injected with 1 μM thiol repeat the measurement at time intervals to obtain the LSPR spectrum.

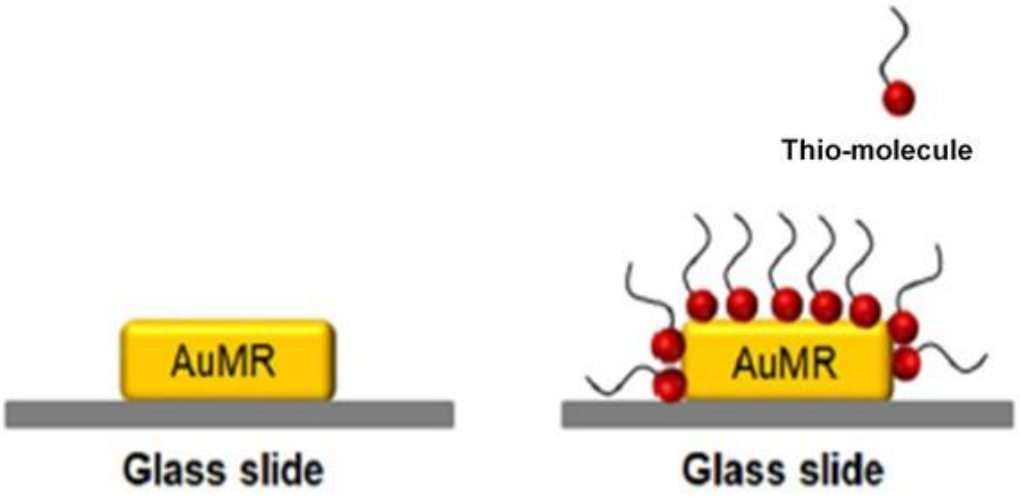

Figure 3. Schematic of the process of attaching chemicals to the surface of metal nanoparticles

2.6. Synthesis of Gold Nanoplates

The one-pot seedless growth synthesis method was adopted to synthesize triangular gold nanoplates (AuNPs). In a 20 mL vial, 1.6 mL of 0.1 M Hexadecyltrimethylammonium chloride (CTAC) was first diluted with 8 mL of ultrapure water, followed by the addition of 100 μL of 0.01M KI. 80 μL of 25.4 mM $HAuCl_4$ and 20.3 μL of 0.1M NaOH were then added into the mixture sequentially. Then, 80 μL of 0.064 M ascorbic acid was injected into the solution with moderate shaking. Finally, 10 μL of 0.1 M NaOH was injected and the flask was quickly shaken for 1–2 s. The growth process can be completed within ~ 10 min [24].

2.7. Optical Characterization and Polarization-Dependence Measurement of Gold Nanoplates

The sample glass slide was placed onto the microscope stage and we attached a polarizer and a 640-nm band-pass filter to the DF microscope condenser in order to characterized optical properties of polarization-dependence. When the focal plane is reached, a DF image of a single AuNPs is obtained while rotating the polarizer at intervals of 10 degrees from 0 to 180 degrees.

3. Result and Discussion

3.1. Defocused Dark-Field Orientation Imaging of Single Gold Microrods on Synthetic Membranes

AuMRs were characterized with scanning electron microscopy (SEM) and their size was determined to be about 200 nm × 1μm. Figure 4A shows a SEM image of single AuMRs. A UV-Vis extinction spectrum of 1-μm AuMRs dispersed in water was obtained using a Varian Cary 300 UV-Vis spectrophotometer (Figure 4B). For micrometer-long AuMRs, the dipole plasmon mode red-shifts while more extinction peaks are observed at shorter wavelengths, corresponding to the longitudinal higher order mode [25-27]. As shown in Figure 4B, higher-order modes appear in the visible spectrum. The sample was prepared by spin casting a solution containing AuMRs on a pre-cleaned glass slide, and the concentration of AuMRs on the glass surface was controlled to facilitate single particle characterization.

According to the electrostatic approximation, plasmon oscillations from an anisotropic AuMR can be simplified as three perpendicular independent oscillations in three axes (Figure 5); oscillation along the long principal axis (a-axis) is defined as a longitudinal mode and the other perpendicular oscillations are defined as transverse modes vibrating along the short axes (b and c axes). E_a indicates the scattering electric field of the microrod along the main long axis, while E_b and E_c are the scattering electric field along the short transverse axes b and c (Figure 5). In this study, the polar

angle θ and the azimuthal angle φ of a AuMR in 3D space are defined as shown in Figure 5. The overall scattering electrical field from a AuMR can be quantified through linear superposition of three independent scattering electric fields associated with three mutually orthogonal oscillations as shown in eqn (1):[22]

$$E_{(\mathrm{scat})} = \sum_{a,b,c} E_{(\mathrm{scat})j} = E_{(\mathrm{scat})a} + E_{(\mathrm{scat})b} + E_{(\mathrm{scat})c} \qquad (1)$$

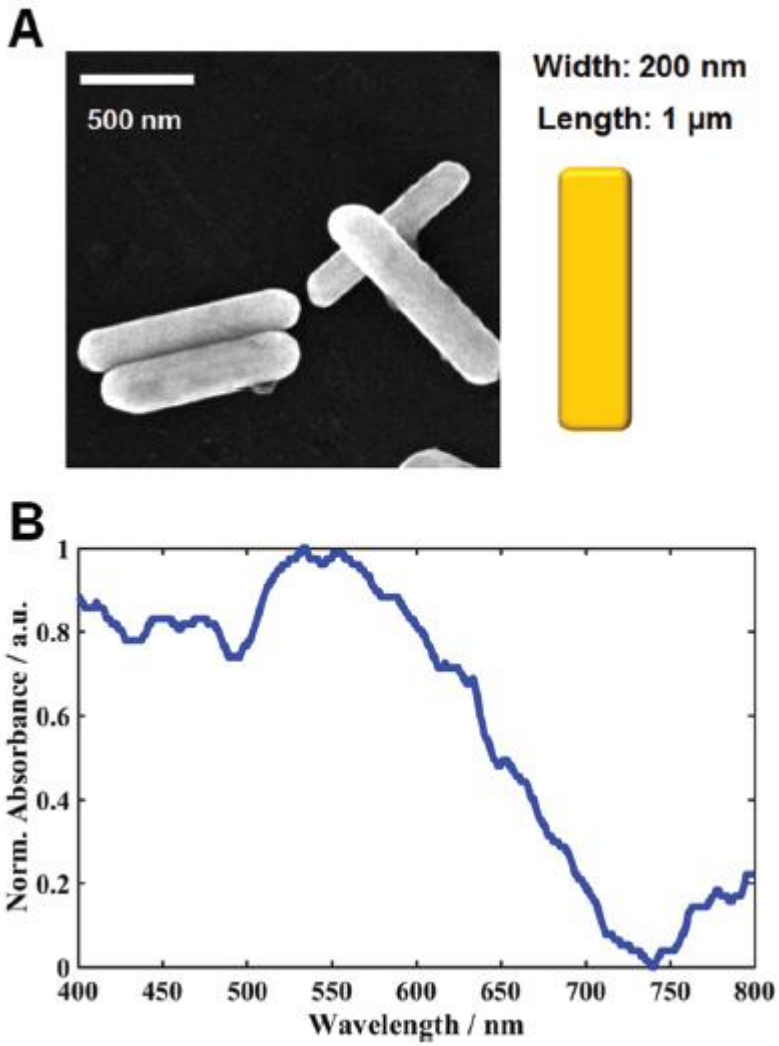

Figure 4. (A) The SEM image of Au microrods. The average length and width of microrods are 1000 nm and 200 nm, respectively (B) UV-Vis absorption spectrum of 1 μm-long Au microrods dispersed in water

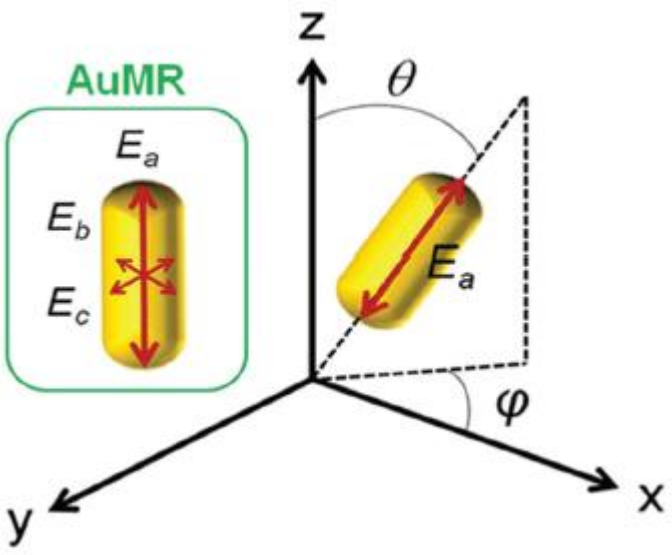

Figure 5. A schematic depicting three-perpendicular oscillations along the three axes. Ea denotes the scattering electric field of the microrod along the main long axis. Definitions of the polar angle θ and the azimuthal angle φ of a microrod in 3D space are also shown

We first obtained the scattering spectra of single AuMRs used in this study. As shown in Figure 6, multipolar LSPR peaks were observed for the AuMRs in the visible spectrum, which is consistent with the ensemble absorption spectrum in Figure 4B. A vertical scan with a step size of ~ 40 nm was then performed to obtain both focused (Figure 7A) and defocused (Figure 7B) images of randomly-orientated AuMRs immobilized on a glass slide. As shown in Figure 7A, the 2D (or in-plane) orientation of single AuMRs was observed in the focused DF image. Furthermore, we found that characteristic doughnut-shaped image patterns with lobes in the peripheral area are observed in the defocused DF scattering image (Figure 7B). Figure 7C shows the DF images of the three AuMRs highlighted in Figure 7A at four different defocusing distances. It is evident that the spatial field distribution of AuMRs in DF microscopy can be resolved when the sample is moved away from the focal plane. The optimum defocusing distance was determined to be ~ 1 μm under the DF microscopy imaging conditions and resulted in the clearest patterns for determining the orientation of AuMRs. At a defocusing distance of 0 μm (i.e., in-focus), a solid bright spot elongated along the main long axis of a AuMR was observed for the three AuMRs. When the imaging plane was moved 1 μm away from the focal plane, a clear doughnut-shaped image pattern appeared with two lobes exhibiting the scattering field distribution and an angular anisotropy. The white-dotted line depicts the orientation of AuMRs. It should be noted that the in-plane orientation angle observed in the defocused DF image at a defocusing distance of 1 μm is ingood agreement with the orientation angle observed in the focused DF image.

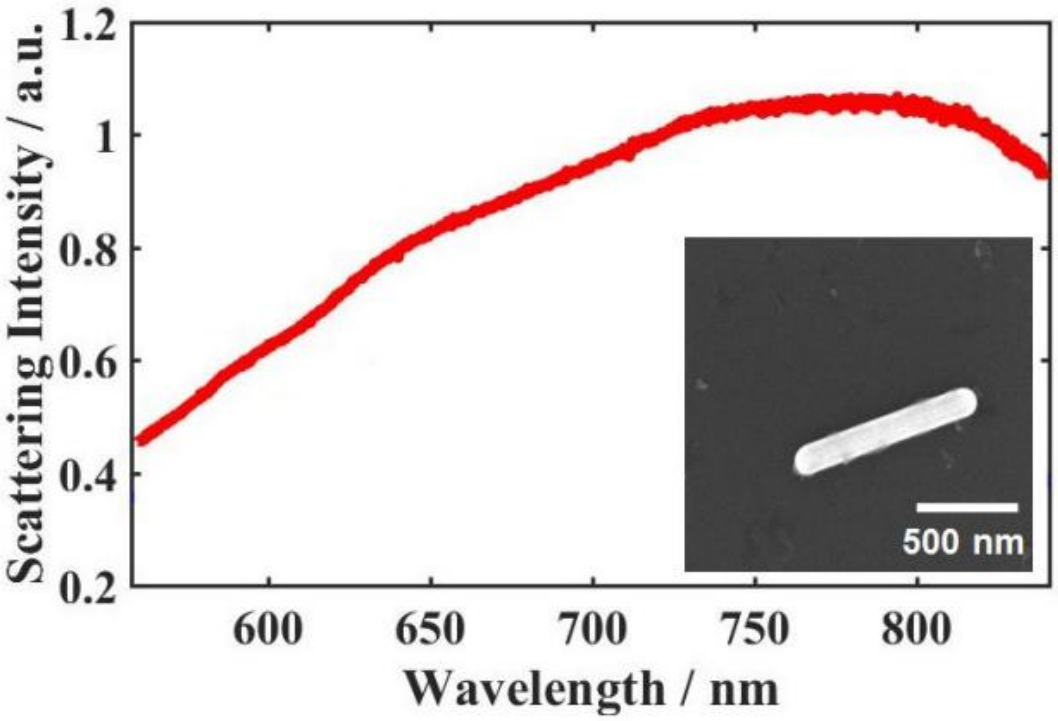

Figure 6. Single particle scattering spectrum of a AuMRs. The inset shows a SEM image of single AuMRs

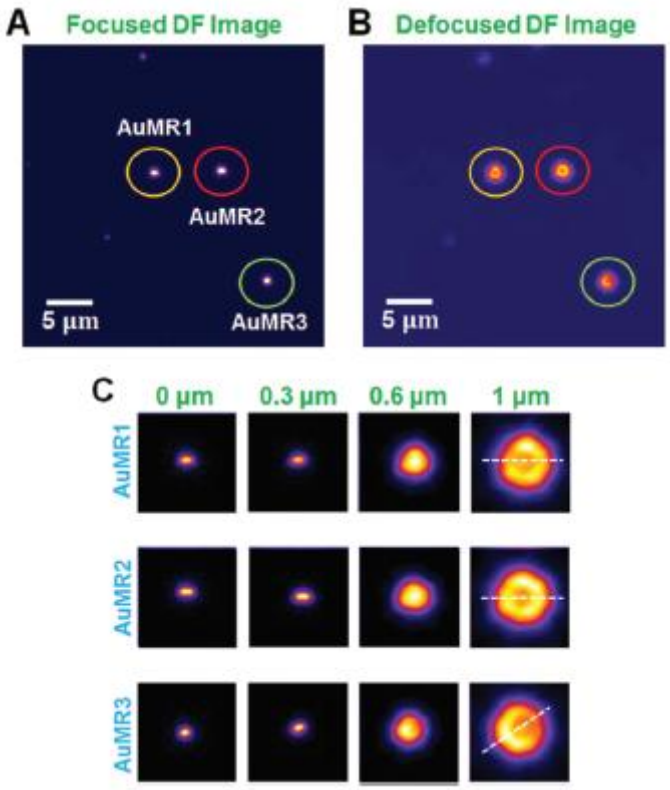

Figure 7. (A) Focused DF scattering image of single AuMRs (B) Defocused DF image of the same microrods in (A) at a defocusing distance of 1 µm (C) DF scattering images at four different defocusing distances of 0 µm (in-focus), 0.3 µm, 0.6 µm and 1 µm

We then tried to confirm if we can directly determine the in-plane and out-of-plane angles of AuMRs from their characteristic spatial scattering intensity distributions. To experimentally verify the capability of resolving the 3D orientation of a AuMR, two single AuMRs with different orientation angles in the Cartesian plane were randomly selected (Figure 8). The measured scattering patterns at a defocusing distance of 1 μm were used to determine the 3D orientation of the AuMRs by fitting with the best-matched simulated patterns. In this study, we used the simulation program developed by Enderlein and Bo¨hmer for calculating the characteristic intensity distribution from an emitter with three perpendicular oscillations of different emission strengths. We found that the measured patterns for the two AuMRs are ingood agreement with the best-matched simulation patterns (Figure 8). The 3D spatial orientations of the two AuMRs were determined through the pattern match analysis. Furthermore, we found that a doughnut-shaped scattering pattern at a polar angle of 0º is circularly symmetric. However, a scattering field torus is no longer circularly symmetric and the center moves toward the edge of a pattern upon increasing the polar angle θ (Figure 8). Therefore, we found that the characteristic scattering patterns can enable us to determine the 3D spatial orientation (or in-plane and out-of-plane angles) of a AuMR.

In this simulation, there are two important parameters of k and R which allow us to define the emission strength ratios of the three perpendicular oscillations in Figure 5. The ratio R defines the emission strength of the a-oscillation (or longitudinal oscillation) to the combined b and c transverse oscillations as shown in eqn (2):

$$R \times I_a + (1 - R) \times (I_b + I_c) \qquad (2)$$

when R is 1, we only have the contribution from a-oscillation (longitudinal oscillation) to the image patterns. However, in the case of large AuMRs, the other two transverse oscillations (b and c) can contribute to the image patterns. We therefore investigated the degree of contribution from the transverse oscillations by decreasing the R value (e.g., from 1 to 0.8). Figure 9 shows the simulated scattering patterns of a AuMR upon varying the parameter R from 1 to 0. In this simulation, the polar angle θ of the AuMR was set to 90º. As shown in Figure 9 it is important to consider the contribution from transverse oscillations to the image patterns of the AuMRs with a thick diameter of 200 nm.

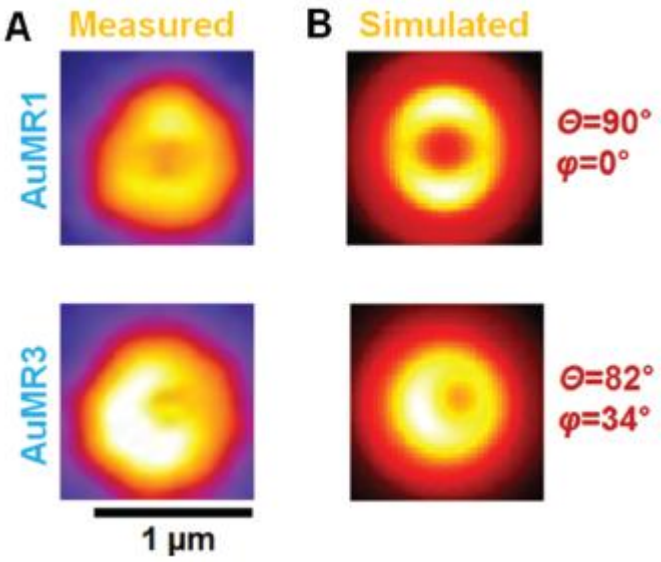

Figure 8. The measured and best-matched simulation patterns from two randomly selected AuMRs in different orientations on a glass slide. The measured patterns (A) are obtained at a defocusing distance of 1 μm. It is shown that the measured patterns (A) match well with the simulated patterns (B). The 3D spatial orientations of the AuMRs were determined through the pattern match analysis. The scale bar represents 1 μm

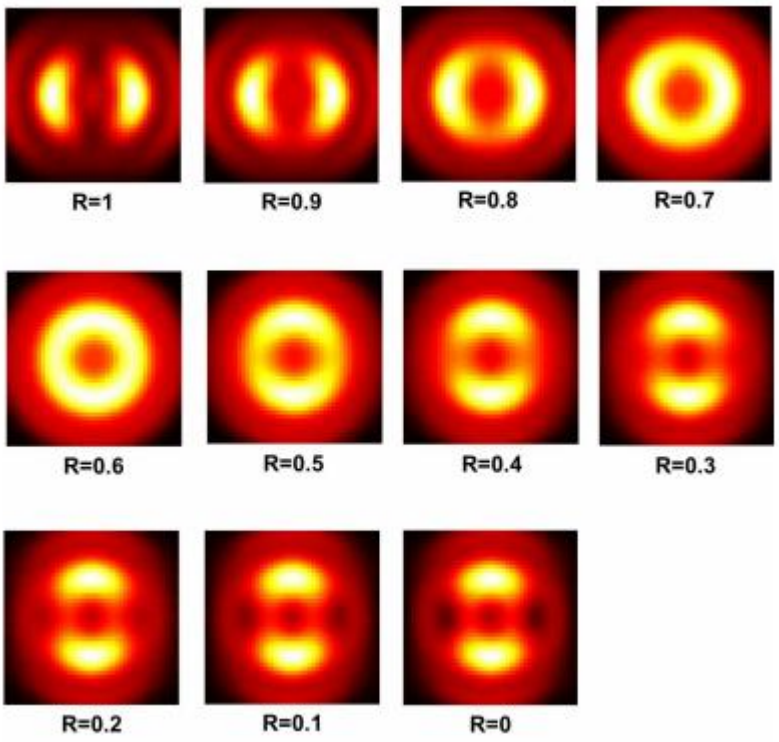

Figure 9. The simulated scattering patterns of a AuMRs by varying the parameter R from 1 to 0 in the focal plane. In this simulation, the polar angle θ of a AuMRs was set to 90°

Finally, we checked if we can track the change in orientation dependent, characteristic defocused scattering patterns of a AuMR in dynamic biological systems as a function of time. In this study, we chose single AuMRs rotating on synthetic membranes as a model system. Cetyltrimethyl ammonium bromide (CTAB) - coated AuMRs freely diffusing in solution when introduced into a chamber can be bound to the membrane through non-specific binding. We recorded movies that show rotational motions of surface-bound AuMRs at a temporal resolution of 100 ms using DF microscopy (Figure 10A). We observed that the doughnut-shaped characteristic patterns changed dynamically as a function of time (Figure 10B). Therefore, we could observe and track the change of the doughnut-shaped scattering pattern of a AuMR bound onto the membrane as a function of time using defocused DF microscopy. The results support that the out-of-plane orientations of single AuMRs rotating on synthetic membranes can be resolved accurately using a defocused DF microscope.

There are two important points that need to be discussed in Figure 10. First, Li et al. reported 3D orientation sensing of gold nanorods by defocused imaging using a two-photon luminescence (TPL) microscope. However, the TPL-based technique requires the use of a strong laser excitation source, which limits its applicability for biological imaging. Therefore, the DF imaging technique used in this study is better suited for biological studies. Second, it is necessary to discuss the dispersion characteristics of AuMRs on synthetic membranes. It should be noted that we can directly observe AuMRs under a DF microscope and distinguish single AuMRs from aggregates from their DF images. We found that AuMRs adsorbed on the membrane

were mostly single particles instead of aggregates. Therefore, in this study we ensured that single AuMRs adsorbed on the membrane were measured using DF microscopy.

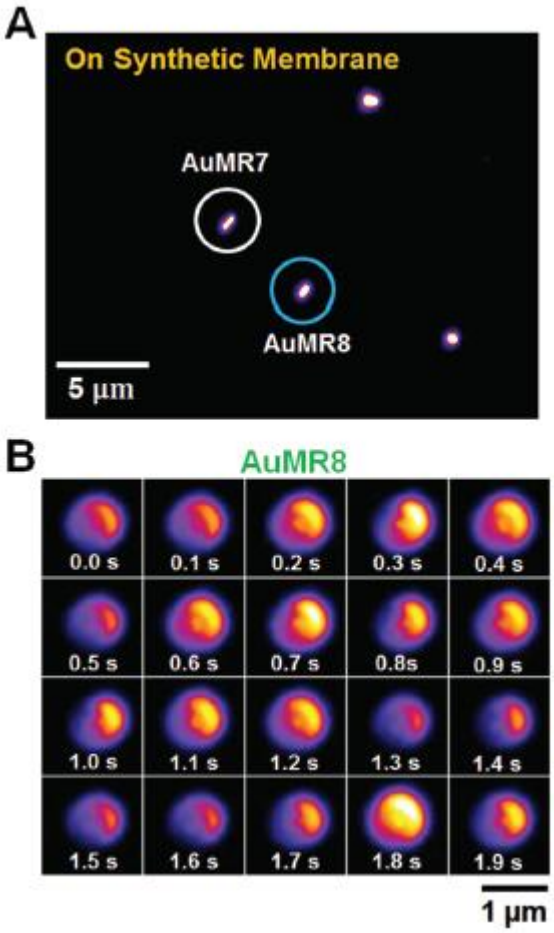

Figure 10. Dynamic tracking of 1 µm long AuMRs on synthetic membranes with defocused DF microscopy. (A) DF image of single AuMRs bound onto the membrane. (B) 20-successive defocused DF scattering images of AuMR8 as a function of time. Temporal resolution is 100 ms

3.2. Chemical Effect on Surface Plasmon Damping in One-Dimensional Single Gold Microrods

In the present study, AuMRs capped by cetyltrimethylammonium bromide (CTAB) were obtained from Sigma-Aldrich (St. Louis, MO, USA). The AuMRs have an average size of 200 nm × 1 μm as observed by a scanning electron microscope (SEM) Figure 11A. An UV–Vis extinction spectrum of the AuMRs dispersed in pure water was obtained with a Varian Cary 300 UV–Vis spectrophotometer (Agilent, Oregon, USA) Figure 11B. For AuMRs, the resonance wavelength is affected by changes in the size, shape, and surrounding environment of the AuMR, and the characteristic higher-order modes are observed in their UV–Vis extinction spectrum. However, the ensemble measurement cannot provide detailed information about the optical properties and plasmon damping of single AuMRs. In this respect, single particle spectroscopic measurement is necessary to better understand their optical properties and chemical interface damping (CID) at the single particle level without ensemble averaging.

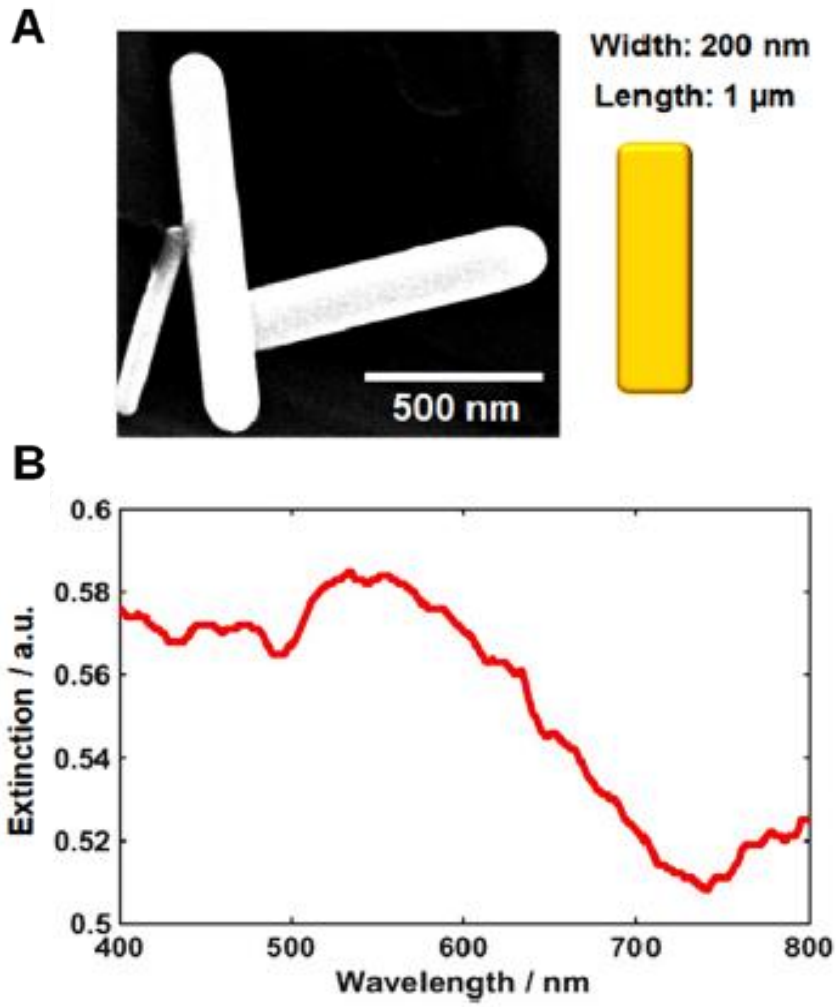

Figure 11. (A) SEM image of single AuMRs with an average size of 200 nm × 1 μm. (B) Extinction spectrum of AuMRs dispersed in water

We performed single particle scattering studies to characterize the CID effect of AuMRs with 1-decanethiol under DF microscopy. As depicted in Figure 12, thiol molecules are known to efficiently adsorb on gold surfaces within minutes by formation of strong covalent gold–sulfur bonds [28-30]. At longer timescales, the thiol molecules attached on the surface reorganize into denser monolayers by the attractive van der Waals interactions between the carbon chains of the thiol molecules [31]. We obtained DF scattering images of single AuMRs before and after the adsorption of 1-decanethiol molecules on the particle surfaces (Figures 12 and Figure 13). Figure 13A shows DF scattering image of single AuMRs immobilized on the glass slide before the adsorption of thiol molecules. It is not able that the in-plane orientation of AuMRs on the glass slide is directly visualized under DF microscopy, and we ensured that single AuMRs were measured in this study. We then attempted to obtain the scattering spectra of single AuMRs in order to have a deeper understanding of their optical properties at the single particle level. Figure 13B shows scattering spectra of AuMR1 (indicated in Figure 11A) before and 30-min after the adsorption of thiol molecules on the particle surface. The single particle scattering spectra of large AuMR1 showed multipolar LPSR peaks, which is consistent with the ensemble spectrum shown in Figure 11B. More importantly, the adsorption of 1-decanethiols on the gold surface caused a significant decrease in the scattering intensity due to the CID effect (Figure 13B). To the best of our knowledge, this is the first study to report the CID effect in large AuMRs at the single particle level under DF microscopy and spectroscopy.

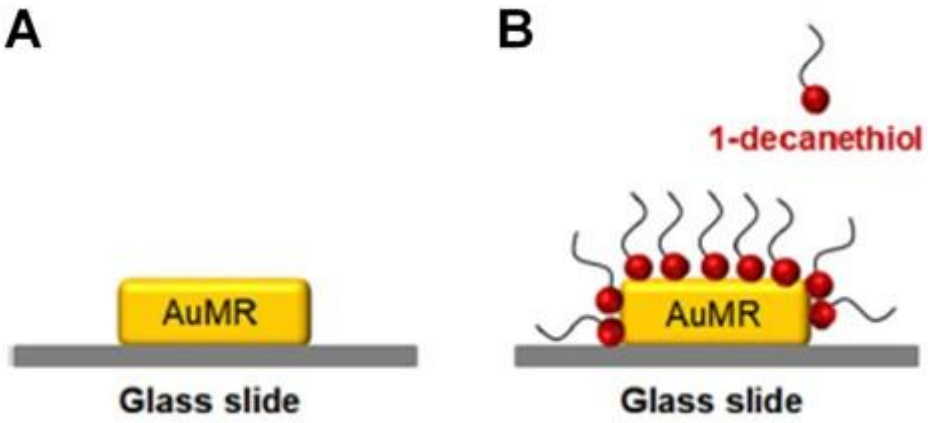

Figure 12. (A) Schematic of single AuMRs in the absence of 1-decanethiol. (B) Schematic of single AuMRs capped with 1-decanethiol. Thiol groups have a strong affinity for gold

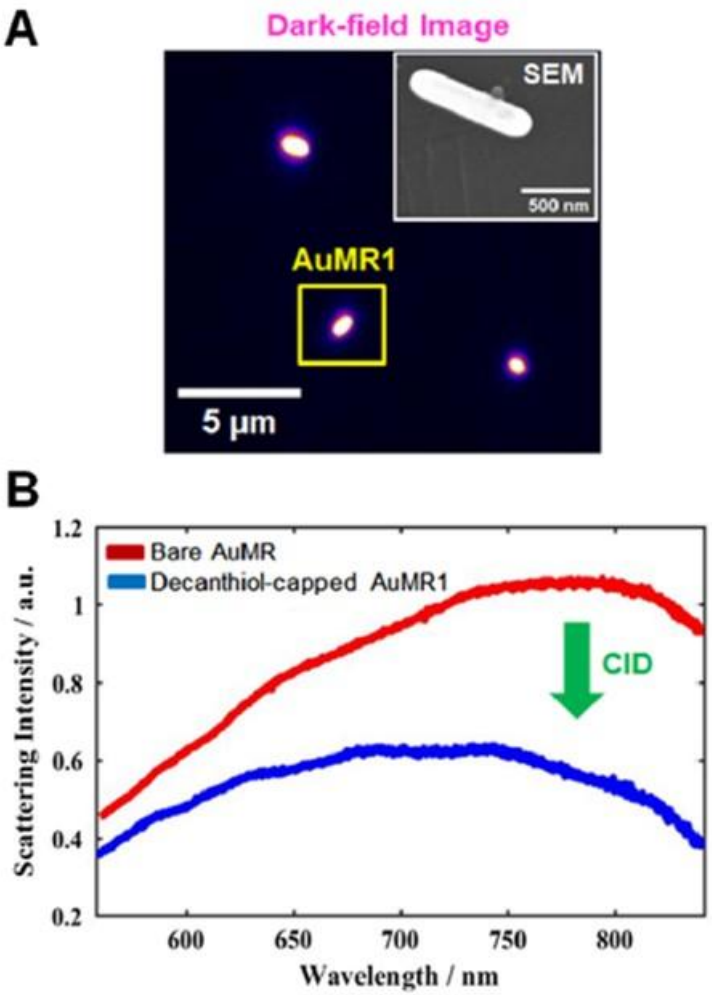

Figure 13. (A) DF scattering image of single AuMRs. Inset shows a SEM image of single AuMR with a length of 1 µm. (B) Scattering spectra of single AuMR1 highlighted in panel (A) in the absence of 1-decanthiol (red curve) or in the presence of 1-decanthiol (blue curve). The scattering spectrum is strongly damped due to CID

We then tried to better understand the effects of electrophilicity of thiol groups on the CID effect in single AuMRs. In this study, two kinds of thiol molecules (4-aminothiophenol and 4-nitrothiophenol) were employed to investigate the thiol effect according to electrophilicity. 4-Aminothiophenol is a strong EDG, while 4-nitrothiophenol is a strong electron EWG. We performed real-time monitoring of molecular binding events on single AuMRs to elucidate the CID effect with adsorbate thiol molecules of different electrophilicity under DF microscopy and spectroscopy. In this study, the scattering spectra of single AuMRs were measured at 2-min intervals after injecting 1 μM of thiol molecules (Figure 14). Figure 15A shows the time dependence of the scattering intensity of single AuMR, measured at 2-min intervals after injecting 1 μM of 4-aminothiophenol molecules (EDG), while Figure 15B shows the time dependence of the scattering intensity of single AuMR after introducing 1 μM of 4-nitrothiophenol molecules (EWG). As shown in Figure 15, the scattering intensity was decreased due to the adsorption of thiol molecules as a function of time. More interestingly, 4-nitrothiophenol with EWG caused a faster plasmon damping of single AuMRs than 4-aminothiophenol with EDG within 5 min and, then, the scattering intensity decreased gradually. The faster damping within 5 min in case of 4-nitrothiophenol can be explained by the formation of adsorbate thiol molecules into denser monolayers as well as a strong electron-withdrawing ability of 4-nitrothiophenol from AuMR. Therefore, the CID was found to be affected by the electrophilicity of adsorbate molecules on the AuMR surface.

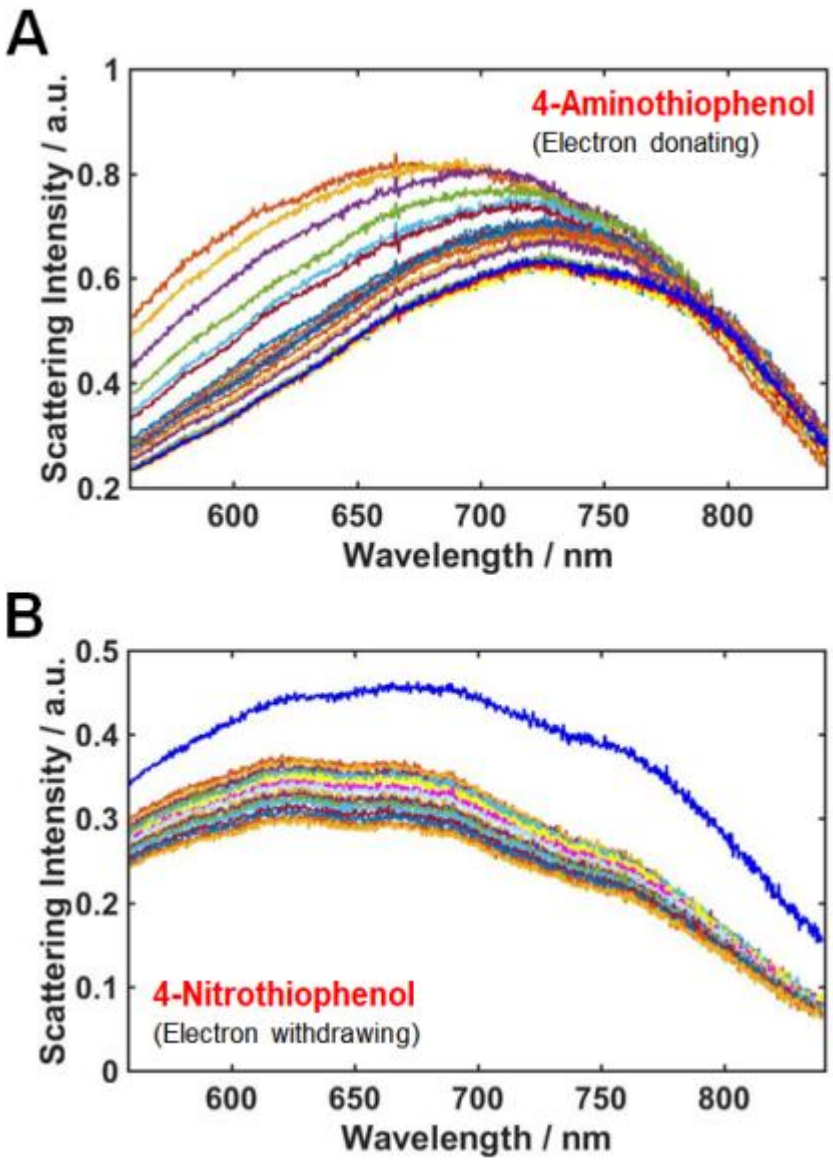

Figure 14. (A) Change in scattering spectra of single AuMRs as a function of time (2-min time intervals) after introducing 1 μM of 4-aminothiophenol strong electron donating group. (B) Change in the scattering spectra of single AuMRs over time (2-min time intervals) after introducing 1 μM of 4-nitrothiophenol strong electron withdrawing group

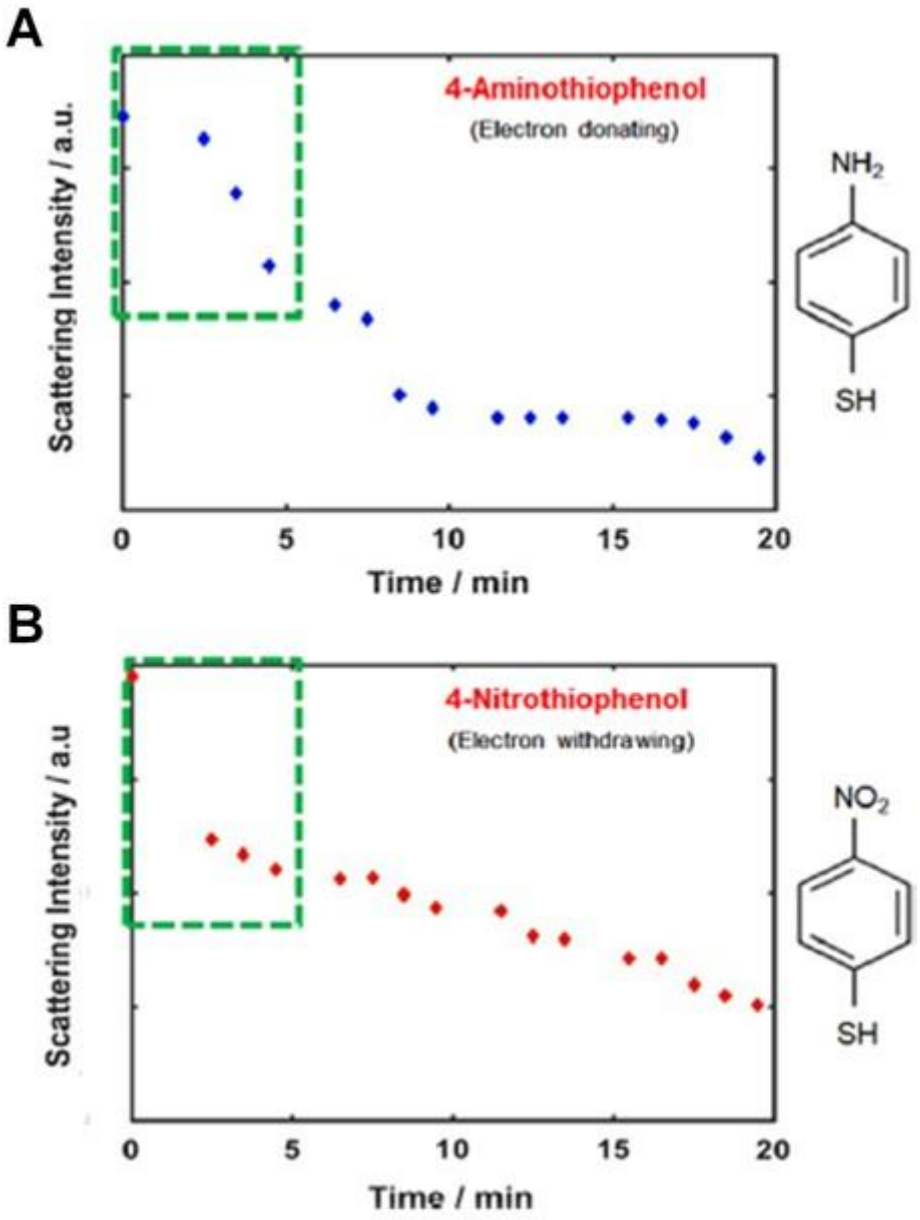

Figure 15. (A) Scattering intensity of single AuMRs as a function of time after adding 4-aminothiophenol with concentration of 1 μM. (B) Scattering intensity of single AuMRs with time intervals of 2 min after introducing 4-nitrothiophenol with concentration of 1 μM.

3.3. Elucidating the Contribution of Dipole Resonance Mode to Polarization-dependent Optical Properties in Single Triangular Gold Nanoplates

Triangular AuNPs were synthesized via a seedless one-pot growth method [24]. Figure 16A shows a SEM image of the synthesized triangular AuNPs, and their average edge length and thickness were determined to be about 100.4(±12.6) nm and 21.1(±3.51) nm, respectively, as depicted in Figure 16B and Figure 17. The thickness was determined by SEM image of single AuNPs standing vertically on the glass substrate (Figure 18). An extinction spectrum of AuNPs was then obtained using UV-Vis spectrophotometer (Figure 19A). For triangular AuNPs, two typical LSPR peaks can be observed in the visible and NIR regions [23, 32-34]. In this study, as shown in Figure 19A, two LSPR peaks were clearly observed for 2D triangular AuNPs at around 540 nm and 630 nm. The two LSPR peaks correspond to quadrupole and dipole resonances, respectively, which arises in the 2D AuNPs as depicted in Figure 19B. In the case of the AuNPs (AR = ~ 5) used in this experiment, the quadrupole peak and the dipole peak were overlapped without complete separation as seen in the UV-Vis spectrum (Figure 19A), which is consistent with the previous theoretical study. Therefore, we experimentally demonstrated that the dipole resonance is not completely separated from the quadrupole resonance for 2D triangular AuNPs with a AR of ～5.

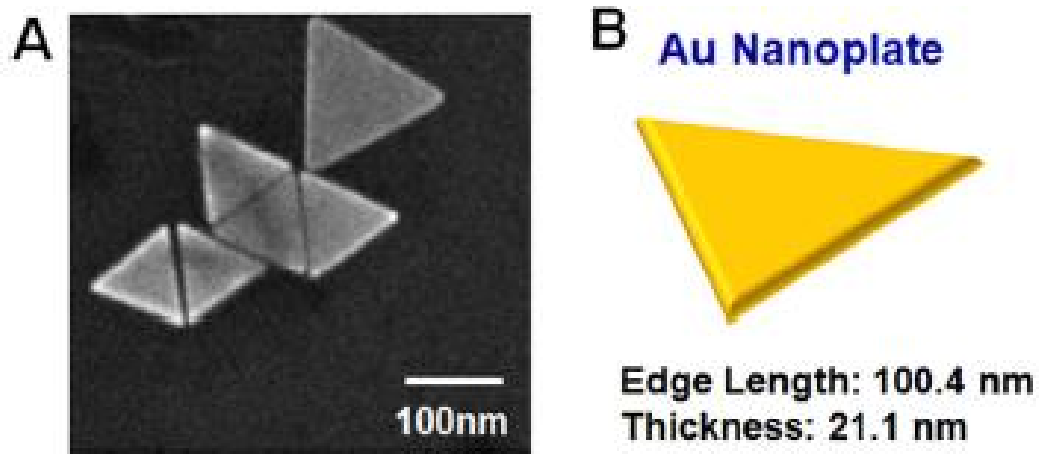

Figure 16. Characterization of triangular AuNPs. (A) SEM image of single AuNPs, (B) Schematic to depict the shape and size of single AuNPs. The average edge length and thickness of single AuNPs were determined to be 100.4 nm and 21.1 nm, respectively

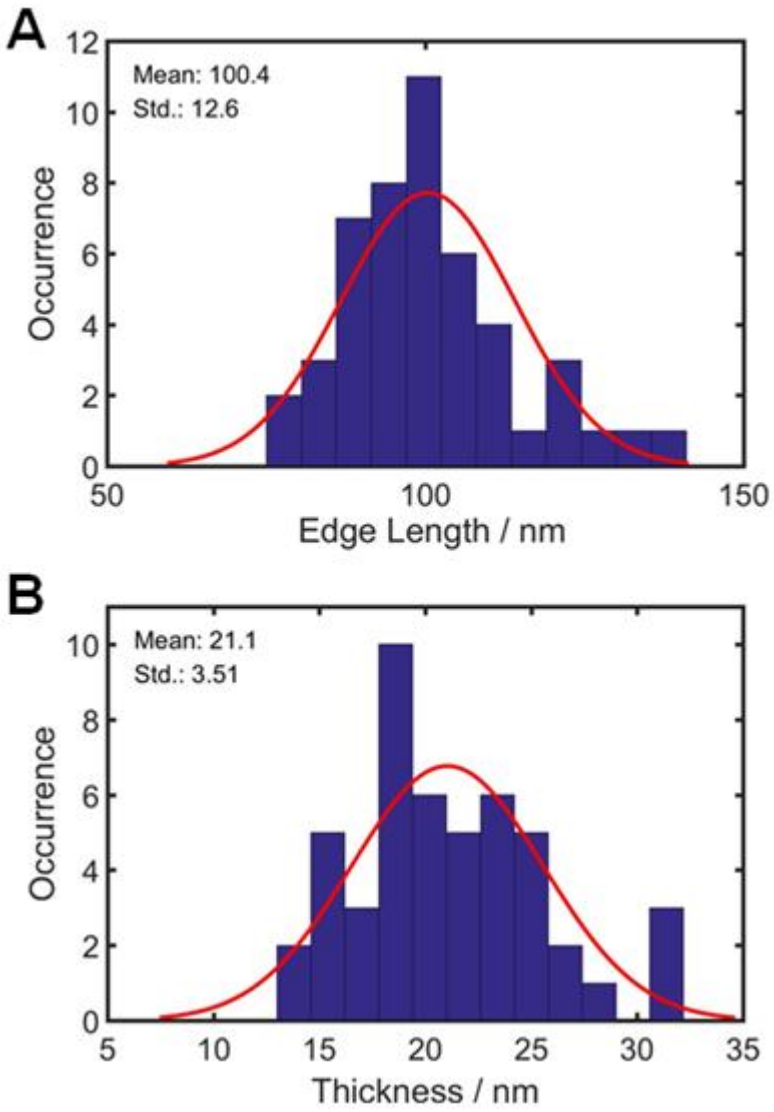

Figure 17. Histograms for (A) edge length and (B) thickness of single AuNPs

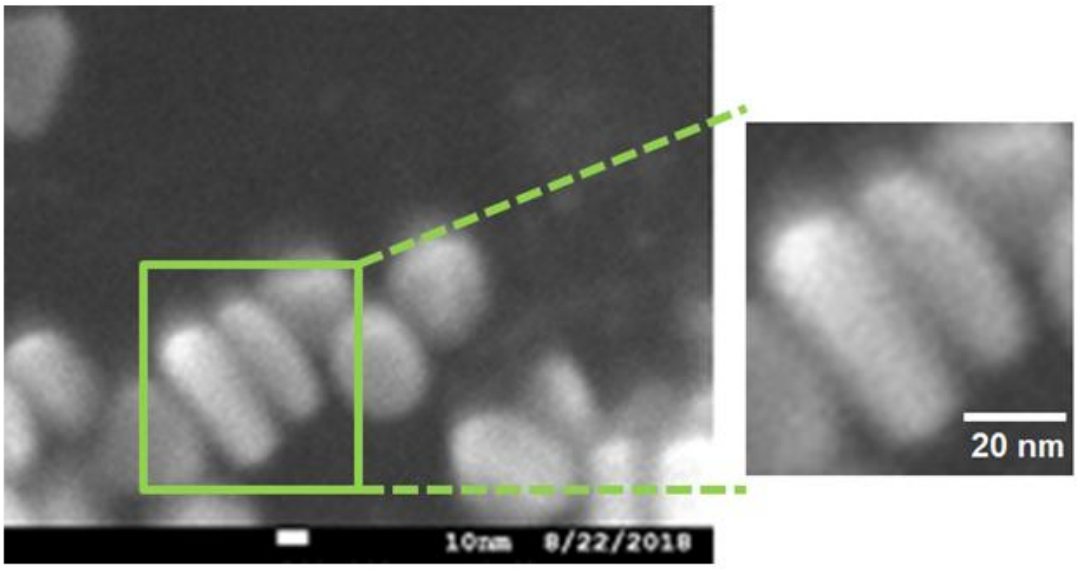

Figure 18. SEM image of AuNPs. Their thickness was determined to be about 20 nm by SEM image of single AuNPs standing up on the glass slide

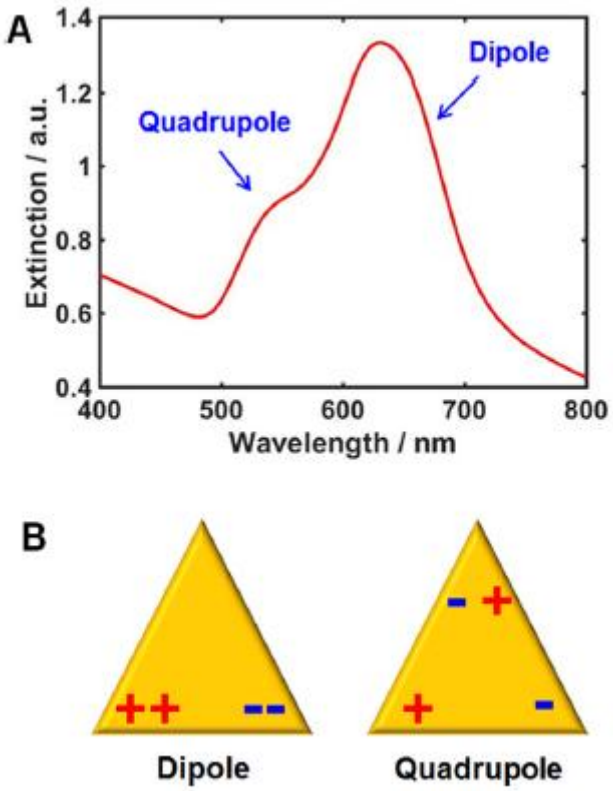

Figure 19. (A) UV-Vis extinction spectrum of 2D triangular AuNPs. (B) Illustration of two typical LSPR resonances in triangular AuNPs.

Figure 20A shows a DF scattering image of single AuNPs obtained at the focal plane. We then obtained single particle scattering spectra of the AuNPs highlighted by a circle in Figure 20A and Figure 20B shows a single particle spectrum of AuNP1 highlighted by a yellow circle in Figure 20A. As shown in Figure 20B, the LSPR linewidth of single AuNP two typical LSPR peaks from dipole resonance and quadrupole resonance were observed in the single particle spectrum. However, the two LSPR peaks were not completely separated, which is consistent with the ensemble spectrum shown in Figure 19A. We further measured single particle scattering spectra of more AuNPs, and the overlapped peaks between dipole resonance and the quadrupole resonance in single AuNPs (AR = ~ 5) were further supported by their single particle spectra to show a broad LSPR peak in between 600 nm and 650 nm (Figure 21). The broad LSPR peak in single AuNPs can be explained by the major contribution from radiation damping among several plasmon decay processes.

We further tested if the spatial scattering field distributions of triangular AuNPs can be visualized and resolved directly from their defocused scattering images. We used a defocused orientation and position imaging (DOPI) technique with the capability of determining the 3D orientation of anisotropic Au nanorod (AuNR) without angular degeneracy. The DOPI techniques are based on the electron transition dipole approximation and the fact that the dipole radiation exhibits an angular anisotropy. The core idea is that the direct detection of the spatial distribution of the scattered or emitted field of single dipoles becomes possible when the imaging system is defocused deliberately by ~ 1 μm. In the present study, the triangular AuNPs were

measured by scanning in the z-direction with a vertical step size of ~ 40 nm. The vertical scan allowed us to obtain both focused and defocused images of single AuNPs deposited on a glass slide at a different defocusing distance. The 2D azimuthal angle φ and polar angle θ of single AuNP can be defined as shown in Figure 22. As shown in Figure 20A, the light scattered from a triangular nanoplate in the focal plane of the objective was focused into a solid bright spot, which provides little information about the spatial scattering field distributions of AuNP. When the 2D triangular AuNP was positioned at ~ 1 μm away from the focal plane, however, characteristic doughnut-shaped scattering patterns were observed with two lobes in the peripheral area (Figure 23). It is notable that the doughnut-shaped image patterns generated for 2D triangular AuNPs are very similar to those seen for 1D single AuNR with a dipole character. Therefore, the result supports that a dipole mode is much more dominant than quadrupole mode in the unseparated LSPR peaks of single AuNPs (AR of ~ 5) measured in this study, which is consistent with the ensemble data shown in Figure 19A and single particle data in Figure 20B. To the best of our knowledge, this is a first report to measure defocused scattering image patterns of 2D single AuNPs for characterizing their spatial field distributions, and to experimentally prove by the DOPI technique that a dipole mode mainly contributes to the overall optical properties of triangular AuNPs with a AR of ~ 5.

Last, to further confirm that 2D AuNPs with a small AR are more affected by dipole mode, we performed polarization-sensitive defocused DF scattering imaging by linearly polarizing the 640-nm excitation beam close to the dipole LSPR mode and

changing the polarization in 10° increments from 0° to 180°. In this study, a polarizer was placed in the light path to measure the polarization dependence of the scattered light. Figure 25 shows a complete set of doughnut-shaped defocused DF scattering images of each AuNP highlighted in Figure 23A as a function of polarization direction at 640 nm. Figure 24A shows defocused DF scattering images of both AuNP2 and AuNP3 with 30° intervals, chosen from the complete set in Figure 25. As shown in Figure 23 and 24A, the doughnut shaped defocused DF image patterns were generated at each polarization angle. However, it is notable that DF scattering intensities of single AuNPs at 640 nm were changed periodically when the polarizer rotated by 10° per step (Figure 24B). In Fig. 24B, the minimum scattering intensity for AuNP2 (red-curve) was seen at ~ 65°. However, the maximum intensity was observed at ~150° when the polarizer was rotated by 90°. There is a phase difference of 90° between the minimum intensity and maximum intensity, which is consistent with the intensity trace for single Au nanorod with a single dipole character. Therefore, we found that the dipole mode contribution is much stronger than that from the quadrupole mode of single AuNPs with a small AR of ~ 5. The result indicates that the dipole mode, despite the triangular 2D nanoparticles, mainly affects the overall scattering properties of single AuNPs when a AR determined by edge length and thickness was less than 5. Therefore, we demonstrated that the LSPR modes in single triangular AuNPs are sensitive to their edge length and thickness. More importantly, we directly visualized and elucidated with the scattering-based DOPI technique the major contribution of dipole resonance to the polarization-dependent optical properties in 2D triangular

AuNPs (AR = ~ 5) with the edges and vertices at the single particle level.

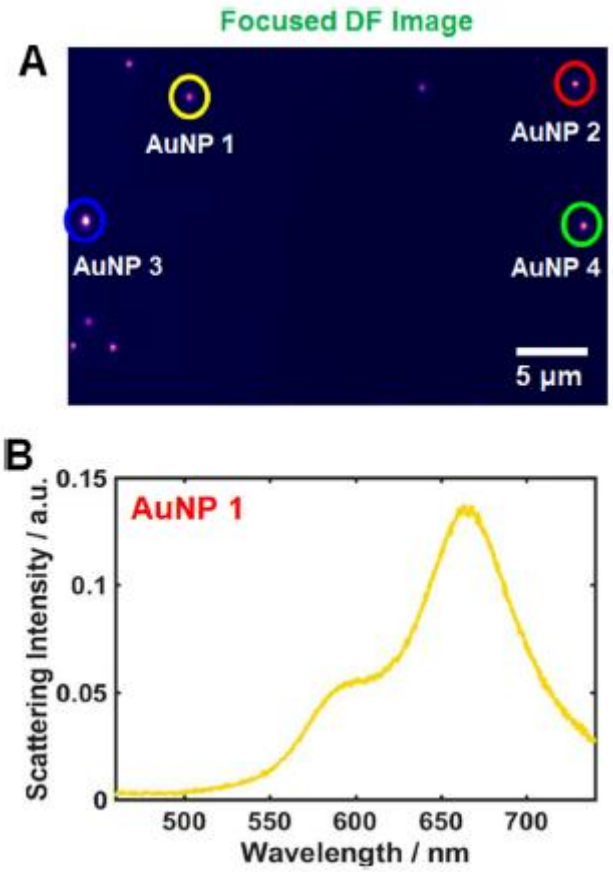

Figure 20. (A) DF scattering image of single AuNPs. (B) Scattering spectrum of single AuNP1 indicated by a yellow circle in (A). Two LSPR peaks are observed at around 590 nm and 660 nm, but not resolved completely

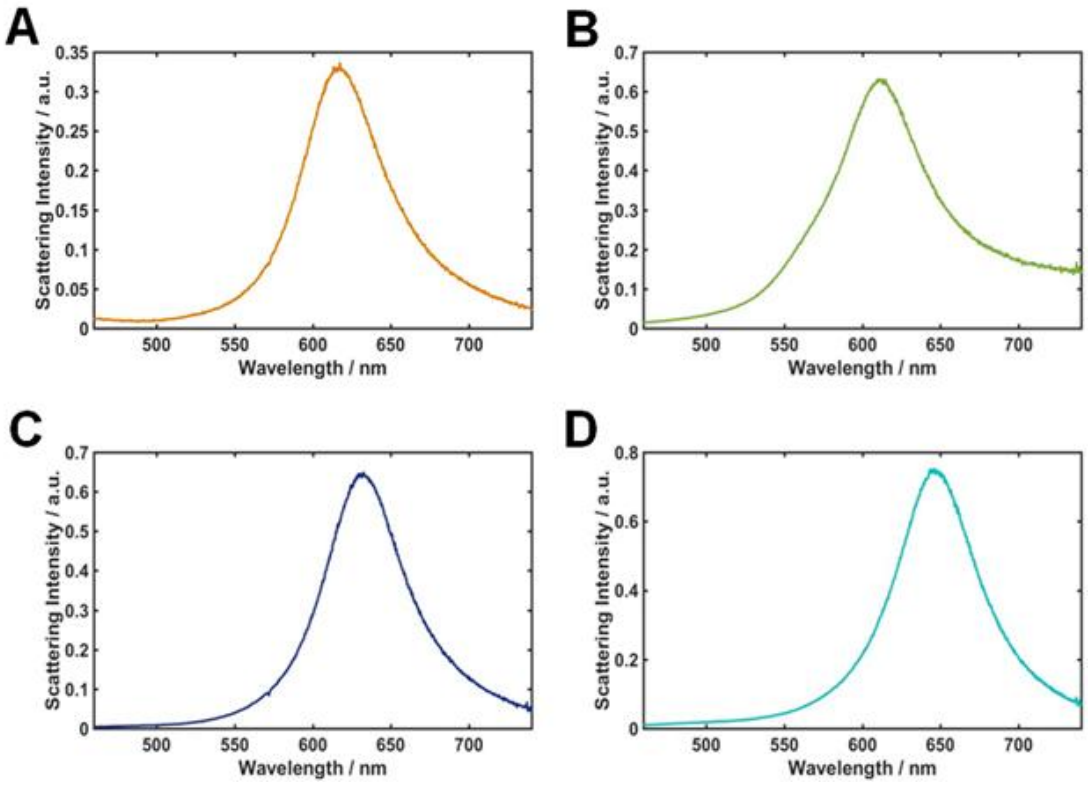

Figure 21. (A-D) Single particle scattering spectra of triangular AuNPs (with a AR of ~5) used in this study. The broad LSPR peak is observed in between 600 nm and 650 nm for single AuNPs

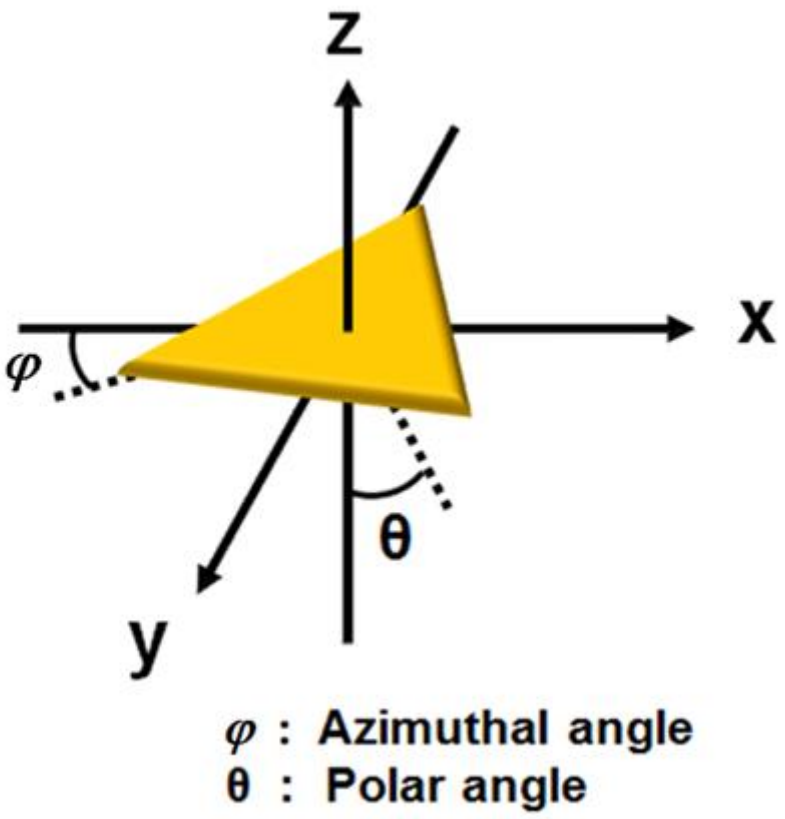

Figure 22. Definition of 3D orientation angles (azimuthal angle φ and polar angle θ) in single triangular AuNPs

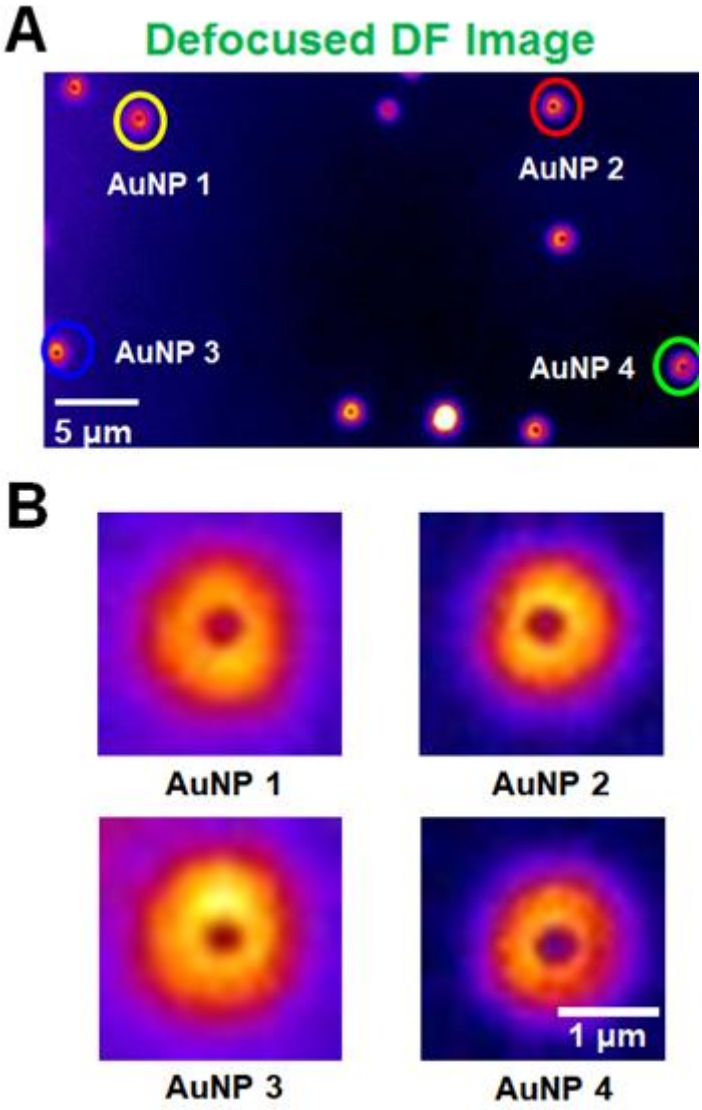

Figure 23. (A) Defocused scattering image of same AuNPs in Fig. 3A obtained at a defocusing distance of ~1 µm under randomly polarized white light illumination. (B) Enlarged defocused image patterns of single AuNPs (AuNP1 to AuNP4). Characteristic doughnut-shaped defocused image patterns appeared

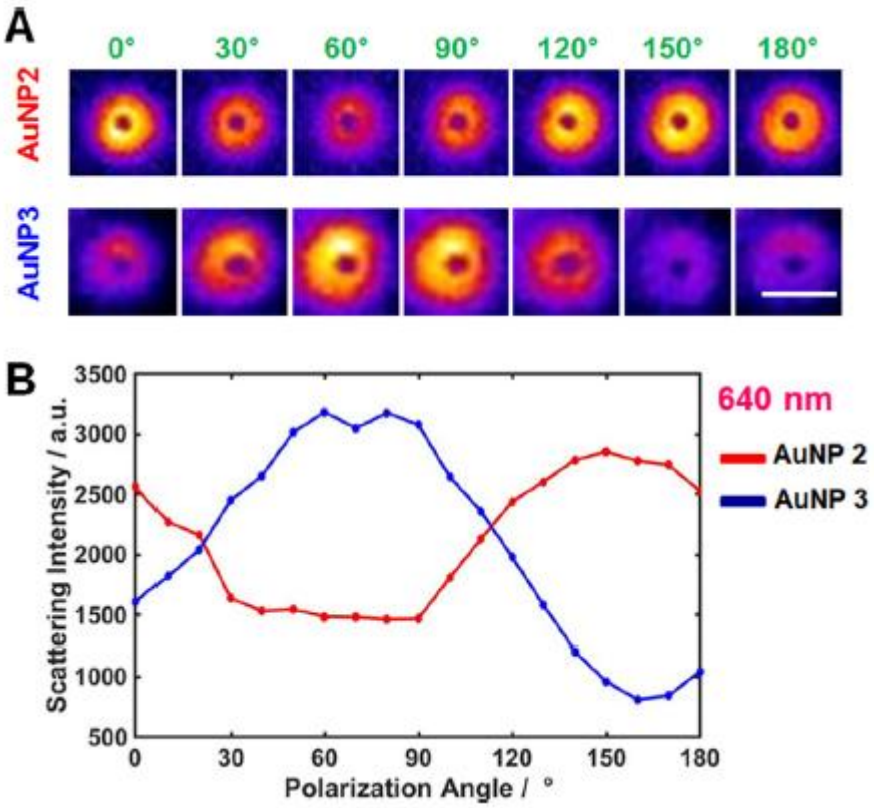

Figure 24. (A) Polarization-dependent defocused image patterns for AuNP2 and AuNP3 under 640-nm linearly polarized light. (B) Change in the scattering intensity for the two AuNPs as a function of polarization angle at 30° intervals

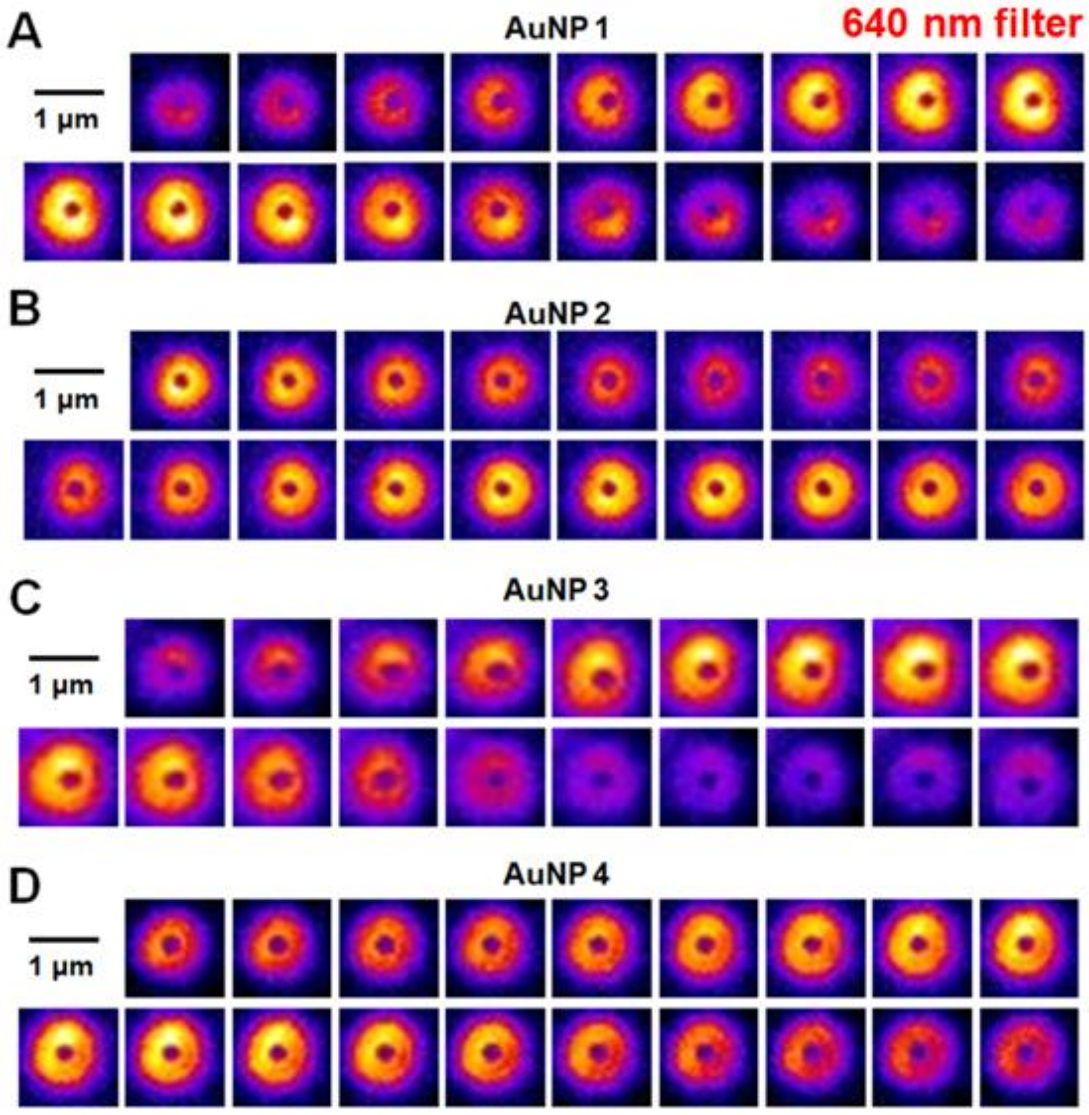

Figure 25. (A-D) Change in the defocused image patterns of 4 single AuNPs indicated in Fig. 3 as a function of polarization angle of incident light at 640 nm from 0° to 180° with 10° intervals. A rotational stage was rotated with 10° intervals to position single AuNPs in different orientations

4. Conclusion

In this study, we analyzed the optical properties of gold nanoparticles using a DF microscope. in the AuMRs study, we further demonstrated that doughnut-shaped defocused scattering patterns of single AuMRs enable us to determine both in-plane and out-of-plane angles of single AuMRs and we present that the defocused orientation imaging technique can be used to track rotational motions and out-of-plane angles of single AuMRs on synthetic membranes. Therefore, we provide a deeper insight into the optical properties of single AuMRs under a defocused DF microscope. The results support the use of the defocused orientation imaging technique in resolving the 3D orientations of single AuMRs in dynamic biological systems. Furthermore, we demonstrated the CID induced by thiol molecules adsorbed on the surface of AuMRs greater than the wavelength of incident light. the adsorbate molecules resulted in a strong decrease of the scattering intensity due to the CID effect in single AuMRs with an average size of 200 nm × 1 μm. We further performed real-time monitoring of molecular binding events on single AuMRs with 4-aminothiophenol strong EDG and 4-nitrothiophenol strong EWG. The CID was affected by the electrophilicity of adsorbate molecules on the nanoparticle surface, and 4-nitrothiophenol with EWG caused a faster plasmon damping of single AuMRs within 5 min. Therefore, we provide a better understanding of the CID in large AuMRs with different thiol molecules at the single particle level.

In the study of AuNP, we carried out a single particle study to characterize the scattering properties of 2D triangular AuNPs with a AR of ~ 5 (edge length: 100.4 nm, thickness: 21.1 nm) synthesized via an one-pot seedless growth method. The positions of dipole peak and quadrupole peak were strongly dependent on the edge length and thickness of single triangular AuNPs, and the dipole resonance was not completely separated from the quadrupole resonance for single AuNPs with a AR of ~ 5. We further used a defocused orientation imaging technique to detect the spatial scattering distributions of emitted fields from dipole and quadrupole modes, which resulted in polarization-dependent, periodic doughnut-shaped scattering patterns and intensities of 2D single AuNPs. Furthermore, we experimentally demonstrated that a dipole mode mainly contribute to the optical properties and polarization dependence of triangular AuNPs with small AR of ~ 5. Therefore, we provided a deeper insight into the optical properties and LSPR modes of single triangular AuNPs at the single particle level, which will be beneficial for their efficient uses in LSPR sensors, photocatalysis, etc.

5. Reference

[1] M. Pelton, J. Aizpurua, G. Bryant, Metal nanoparticle plasmonics, Laser & Photonics Reviews 2 (2008) 136-159.

[2] V. Rai, A. Srivastava, C. Mukherjee, S. Deb, Localized surface plasmon resonance and refractive index sensitivity of vacuum-evaporated nanostructured gold thin films, Indian Journal of Physics 90 (2016) 107-116.

[3] W. Sun, N. Fang, B.G. Trewyn, M. Tsunoda, I.I. Slowing, V.S. Lin, E.S. Yeung, Endocytosis of a single mesoporous silica nanoparticle into a human lung cancer cell observed by differential interference contrast microscopy, Analytical and bioanalytical chemistry 391 (2008) 2119.

[4] Q. Zhang, F. Liu, K.T. Nguyen, X. Ma, X. Wang, B. Xing, Y. Zhao, Multifunctional mesoporous silica nanoparticles for cancer targeted and controlled drug delivery, Advanced Functional Materials 22 (2012) 5144-5156.

[5] X. Wu, T. Ming, X. Wang, P. Wang, J. Wang, J. Chen, High-photoluminescence-yield gold nanocubes: for cell imaging and photothermal therapy, Acs Nano 4 (2009) 113-120.

[6] M. Xuan, J. Shao, L. Dai, J. Li, Q. He, Macrophage cell membrane camouflaged Au nanoshells for in vivo prolonged circulation life and enhanced cancer photothermal therapy, ACS applied materials & interfaces 8 (2016) 9610-9618.

[7] R. Jorgenson, S. Yee, A fiber-optic chemical sensor based on surface plasmon resonance, Sensors and Actuators B: Chemical 12 (1993) 213-220.

[8] E.M. Larsson, J. Alegret, M. Käll, D.S. Sutherland, Sensing characteristics of NIR localized surface plasmon resonances in gold nanorings for application as ultrasensitive biosensors, Nano letters 7 (2007) 1256-1263.

[9] N. Nath, A. Chilkoti, Label-free biosensing by surface plasmon resonance of nanoparticles on glass: optimization of nanoparticle size, Analytical Chemistry 76 (2004) 5370-5378.

[10] J.W. Ha, W. Sun, G. Wang, N. Fang, Differential interference contrast polarization

anisotropy for tracking rotational dynamics of gold nanorods, Chemical Communications 47 (2011) 7743-7745.
[11] C. Sönnichsen, A.P. Alivisatos, Gold nanorods as novel nonbleaching plasmon-based orientation sensors for polarized single-particle microscopy, Nano letters 5 (2005) 301-304.
[12] M.R. Langille, M.L. Personick, J. Zhang, C.A. Mirkin, Defining rules for the shape evolution of gold nanoparticles, Journal of the American Chemical Society 134 (2012) 14542-14554.
[13] D.E. Mustafa, T. Yang, Z. Xuan, S. Chen, H. Tu, A. Zhang, Surface plasmon coupling effect of gold nanoparticles with different shape and size on conventional surface plasmon resonance signal, Plasmonics 5 (2010) 221-231.
[14] F.K. Guedje, M. Giloan, M. Potara, M. Hounkonnou, S. Astilean, Optical properties of single silver triangular nanoprism, Physica Scripta 86 (2012) 055702.
[15] C. Noguez, Surface plasmons on metal nanoparticles: the influence of shape and physical environment, The Journal of Physical Chemistry C 111 (2007) 3806-3819.
[16] W.-S. Chang, J.W. Ha, L.S. Slaughter, S. Link, Plasmonic nanorod absorbers as orientation sensors, Proceedings of the National Academy of Sciences (2010).
[17] J.W. Ha, W. Sun, A.S. Stender, N. Fang, Dual-wavelength detection of rotational diffusion of single anisotropic nanocarriers on live cell membranes, The Journal of Physical Chemistry C 116 (2012) 2766-2771.
[18] K. Marchuk, N. Fang, Three-dimensional orientation determination of stationary anisotropic nanoparticles with sub-degree precision under total internal reflection scattering microscopy, Nano letters 13 (2013) 5414-5419.
[19] T. Shegai, B. Brian, V.D. Miljkovic, M. Kall, Angular distribution of surface-enhanced Raman scattering from individual Au nanoparticle aggregates, Acs Nano 5 (2011) 2036-2041.
[20] H. Xu, M. Käll, Polarization Dependent Surface Enhanced Raman Spectroscopy of Isolated Silver Nanoaggregates, ChemPhysChem 4 (2003) 1001-1005.
[21] E. Toprak, J. Enderlein, S. Syed, S.A. McKinney, R.G. Petschek, T. Ha, Y.E. Goldman, P.R. Selvin, Defocused orientation and position imaging (DOPI) of myosin

V, Proceedings of the National Academy of Sciences 103 (2006) 6495-6499.
[22] L. Xiao, Y. Qiao, Y. He, E.S. Yeung, Three dimensional orientational imaging of nanoparticles with darkfield microscopy, Analytical chemistry 82 (2010) 5268-5274.
[23] K.L. Shuford, M.A. Ratner, G.C. Schatz, Multipolar excitation in triangular nanoprisms, The Journal of chemical physics 123 (2005) 114713.
[24] L. Chen, F. Ji, Y. Xu, L. He, Y. Mi, F. Bao, B. Sun, X. Zhang, Q. Zhang, High-yield seedless synthesis of triangular gold nanoplates through oxidative etching, Nano letters 14 (2014) 7201-7206.
[25] E.R. Encina, E.A. Coronado, Resonance conditions for multipole plasmon excitations in noble metal nanorods, The Journal of Physical Chemistry C 111 (2007) 16796-16801.
[26] B.N. Khlebtsov, N.G. Khlebtsov, Multipole plasmons in metal nanorods: scaling properties and dependence on particle size, shape, orientation, and dielectric environment, The Journal of Physical Chemistry C 111 (2007) 11516-11527.
[27] E.K. Payne, K.L. Shuford, S. Park, G.C. Schatz, C.A. Mirkin, Multipole plasmon resonances in gold nanorods, The Journal of Physical Chemistry B 110 (2006) 2150-2154.
[28] F.T. Arce, M. Vela, R. Salvarezza, A. Arvia, Dynamic characteristics of adsorbed monolayers of 1-dodecanethiol on gold (111) terraces from in-situ scanning tunneling microscopy imaging, Electrochimica acta 44 (1998) 1053-1067.
[29] T. Kondo, M. Yanagida, K. Shimazu, K. Uosaki, Determination of thickness of a self-assembled monolayer of dodecanethiol on Au (111) by angle-resolved X-ray photoelectron spectroscopy, Langmuir 14 (1998) 5656-5658.
[30] M.D. Porter, T.B. Bright, D.L. Allara, C.E. Chidsey, Spontaneously organized molecular assemblies. 4. Structural characterization of n-alkyl thiol monolayers on gold by optical ellipsometry, infrared spectroscopy, and electrochemistry, Journal of the American Chemical Society 109 (1987) 3559-3568.
[31] D.K. Schwartz, Mechanisms and kinetics of self-assembled monolayer formation, Annual Review of Physical Chemistry 52 (2001) 107-137.
[32] W. Hermoso, T.V. Alves, C.C. de Oliveira, E.G. Moriya, F.R. Ornellas, P.H.

Camargo, Triangular metal nanoprisms of Ag, Au, and Cu: modeling the influence of size, composition, and excitation wavelength on the optical properties, Chemical Physics 423 (2013) 142-150.
[33] Z. Li, Y. Yu, Z. Chen, T. Liu, Z.-K. Zhou, J.-B. Han, J. Li, C. Jin, X. Wang, Ultrafast third-order optical nonlinearity in Au triangular nanoprism with strong dipole and quadrupole plasmon resonance, The Journal of Physical Chemistry C 117 (2013) 20127-20132.
[34] Y.Y. Tanaka, T. Shimura, Tridirectional polarization routing of light by a single triangular plasmonic nanoparticle, Nano letters 17 (2017) 3165-3170.